



Bias-free synthesis of hydrogen peroxide from photo-driven oxygen reduction reaction using N-doped γ -graphyne catalyst

Qiaodan Li ^{a,d,1}, Yang Chen ^{a,1}, Feng Du ^{c,d}, Xiaoli Cui ^{a,*}, Liming Dai ^{b,d,**}

^a Department of Materials Science, Fudan University, Shanghai 200433, China

^b Australian Carbon Materials Centre (A-CMC), School of Chemical Engineering, University of New South Wales, Sydney, NSW 2052, Australia

^c Institute of Advanced Materials, School of Chemistry and Chemical Engineering, Southeast University, Nanjing 211189, China

^d Department of Macromolecular Science and Engineering, Case Western Reserve University, Cleveland, OH 44106, USA



ARTICLE INFO

Keywords:

N-doped γ -graphyne
Hydrogen peroxide
Photo-driven ORR

ABSTRACT

It is an ideal route to generate hydrogen peroxide (H_2O_2) via selective $2e^-$ ORR powered directly by sunlight. In this work, we synthesized a metal-free N-doped γ -graphyne catalyst and wired it with n-type semiconductor photoanodes. The introduction of sunlight could lower the onset bias of oxygen reduction reaction (ORR) up to 0.32 V and H_2O_2 was steadily produced without any sacrificial agents and bias. The $2e^-$ ORR selectivity of N-doped γ -graphyne catalyst was bias dependent, and it reached about 74% at 0 bias in 0.1 mol·L⁻¹ KOH. Theoretical calculations showed that in-situ pyridinic-N in N-doped γ -graphyne acted as the active site for ORR, accelerating the rate-determining step of proton abstraction. The H_2O_2 yield reached as high as 7.47 mmol·h⁻¹g⁻¹, outperformed the reported traditional photocatalytic syntheses of H_2O_2 .

1. Introduction

Hydrogen peroxide (H_2O_2) is a green and convenient oxidant [1,2] as well as a potential energy source for fuel cells [3,4]. It has been widely utilized for bleaching, sterilization, organic synthesis, and environmental remediation [5,6]. Compared with the commercial anthraquinone method [7,8], experimental synthesis from H_2 and O_2 over noble metal catalysts (Au, Pd, and Pt) [9,10], and $2e^-$ electrocatalytic ORR [11–13], semiconductor photocatalysis, involving only H_2O and O_2 , is a burgeoning and ideal way for H_2O_2 production [14]. However, traditional photocatalytic systems suffer from serious back reaction and hole trapping agents are usually necessary.

The combination of electrocatalysis and photoelectrochemical (PEC) is an inspiring route that shares the advantages of solar-driving and suppresses back reaction. In this context, Fan and Cui et al. designed a PEC cell in tandem with a single perovskite solar cell device and achieved a solar-to-hydrogen conversion efficiency of up to 6.2% [15]. Glowacki et al. designed PEC cells that separated two half-reactions to address the loss of H_2O_2 and an H_2O_2 concentration of 3 mmol·L⁻¹ was achieved [16]. Chen et al. combined Zn-air battery with a

polytrithiophene photocathode and boosted the output voltage from 1.38 V to 1.78 V [17]. Reisner et al. constructed a photosystem II by wiring dye-sensitized photoanode to hydrogenase for water splitting [18]. Xuan et al. [19] and Ryu et al. [20] employed both photoanode and photocathode for PEC water splitting. Li et al. introduced light and polyterthiophene electrode into H_2O_2 fuel cells and the onset potential shifted from 0.66 to 1.34 V [21]. They further constructed a NiFeO_x/BiVO₄-polyterthiophene dual-photoelectrode system to achieve a high H_2O_2 concentration of 110 mmol·L⁻¹ [22].

Herein, a dual-electrode bias-free solar-driven device was run in 0.1 mol·L⁻¹ KOH solution without any sacrificial agents. As displayed in Scheme 1a, n-type semiconductor and oxygen reduction reaction (ORR) electrocatalyst were employed as the photoanode and cathode, respectively. Under the irradiation of light, photo-induced holes and electrons were generated on n-type semiconductor photoanodes. Oxygen evolution reaction (OER) was driven by the photo-induced holes from n-type semiconductor photoanode while the photo-induced electrons would transport to the cathode to reduce oxygen into H_2O_2 . Compared with electrocatalytic ORR (Scheme 1b), the introduced light could lower the onset bias of ORR so that external power source was no longer essential.

* Corresponding author.

** Corresponding author at: Australian Carbon Materials Centre (A-CMC), School of Chemical Engineering, University of New South Wales, Sydney, NSW 2052, Australia.

E-mail addresses: xiaolicui@fudan.edu.cn (X. Cui), l.dai@unsw.edu.au (L. Dai).

¹ QiaodanLi and Yang Chen contributed equally to this work.

In comparison with traditional photocatalytic H_2O_2 generation (**Scheme 1c**), the dual-working-electrode system would promote the separation of photo-induced carriers and avoid the reversible reaction of H_2O_2 decomposition.

γ -graphyne is a new two-dimensional (2D) carbon allotrope that consists of sp-hybridized and sp^2 -hybridized carbon [23,24]. We have synthesized γ -graphyne for the first time through a mechanochemistry method [25], and applied it in the field of photocatalysis [26,27], electrocatalytic oxygen evolution [28], and lithium-ion batteries [29,30]. In this work, N-doped γ -graphyne was mechanosynthesized and the ORR 2e^- selectivity was demonstrated by rotating disk electrode (RDE) technique. The ORR 2e^- selectivity of N-doped γ -graphyne depended strongly on the applied potential. Employing the photo-induced electrons of TiO_2 electrode as driving force, the onset bias of ORR was lowered up to 0.32 V to efficiently generate H_2O_2 under no bias with a H_2O_2 selectivity of about 74%.

2. Experimental details

2.1. Synthesis of N-doped γ -graphyne

A mechanochemical route was implemented to fabricate N-doped γ -graphyne. Typically, 2 mL benzene, 0.15 mL pyridine, 10.0 g CaC_2 , 35 mL absolute ethanol were mixed in a stainless-steel pot (250 mL) with 375 g stainless steel balls. The pot was sealed and rotated by a planetary ball mill (TENCAN QXQM-2, China) at 600 rpm for 8 h, then at 450 rpm for another 8 h. To avoid overheating, a cooling interval of 15 min was implemented every 30 min during the milling. After ball milling, the obtained slurry was annealed in N_2 at 260 °C for 3 h. The annealed solid was etched by dilute nitric acid (0.1 mol·L⁻¹) several times under ultrasonic treatment until no Fe^{3+} could be detected in the etching solution. Finally, the purified N-doped γ -graphyne was separated by centrifugation and drying. The calculated molar ratio of N was about 0.6% in the as-prepared N-doped γ -graphyne according to the stoichiometric proportion.

The general chemicals, pretreatments, and characterization details for the samples are provided in [Supporting Information](#).

2.2. Fabrication of N-doped γ -graphyne electrodes

1.6 mg as-prepared N-doped γ -graphyne was weighted and dispersed in 50 mL H_2O and 100 mL 5 wt% Nafion solution by ultrasonic agitation. Then 5 μL N-doped γ -graphyne glue was dropped onto rotating disk electrodes (5 mm in diameter) supplied by Pine Instrument Company, and 2 μL N-doped γ -graphyne glue was dropped onto CHI-104 glassy carbon electrode (3 mm in diameter) supplied by CHI Company. Both

support electrodes were previously polished by alumina slurries (0.05 μm), ultrasound washed in 50% ethanol solution, dried under nitrogen gas, and finally calibrated with $\text{Fe}(\text{CN})_6^{3-}/\text{Fe}(\text{CN})_6^{4-}$ redox couples.

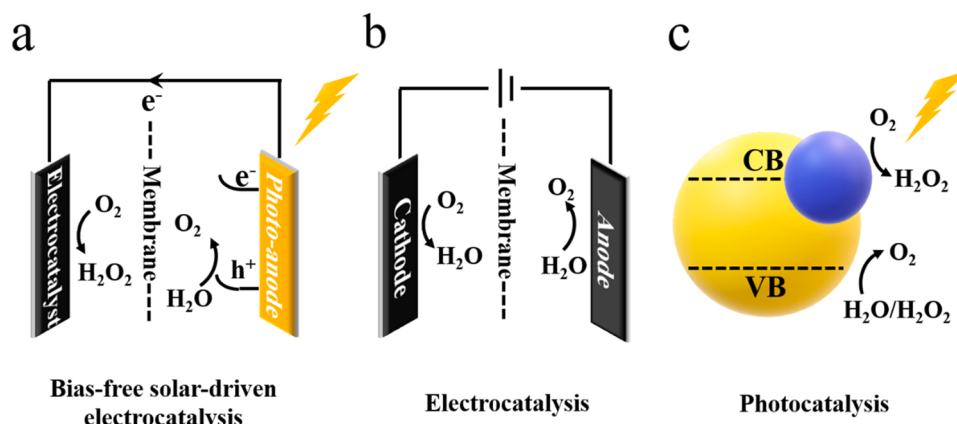
2.3. Electrochemical measurements

A PLS-SXE300BF Xe lamp from PerfectLight Company was selected as the light source for photoelectrochemical measurements. The pristine ORR performance of N-doped γ -graphyne was implemented by a three-electrode system on a CHI-760 electrochemical workstation, using N-doped γ -graphyne@RDE as the working electrode, graphite rod (99.9999%) as the counter electrode, and Hg/HgO electrode as the reference electrode. The ORR performance of N-doped γ -graphyne under the driven of photoinduced electrons was characterized by a dual-electrode system on a CHI-760 electrochemical workstation, using N-doped γ -graphyne@RDE as working electrode and TiO_2 with different areas as counter and reference electrodes. The H_2O_2 generation performance of the device was implemented in a CH2010 H-type electrolytic cell with an F-type aeration tube purchased from Tianjin Aida Hengsheng Science-Technology Development Co., Ltd. An N117 Nafion membrane (proton exchange membrane) from Dupont Company was employed to separate the H-type electrolytic cell. N-doped γ -graphyne@glassy carbon was used as working electrode and a 2 cm × 2 cm TiO_2 was chosen as counter and reference electrode. The linear sweep voltammograms (LSV), cyclic voltammograms (CV), and amperometric current-time curves of the dual-electrode device were tested on a CHI-660 electrochemical workstation at 0 bias.

3. Results and discussion

3.1. Characterization of N-doped γ -graphyne

The elementary composition and chemical structure of N-doped γ -graphyne were systematically characterized by EDX, Raman spectroscopy, and XPS. **Fig. 1a** displays a typical EDX spectrum for the N-doped γ -graphyne sample, in which the molar ratio of carbon was 98.38%. Raman spectrum was also employed to characterize the bond structure in the as-prepared sample (**Fig. 1b**). The bands at around 1836 cm^{-1} and 1971 cm^{-1} are attributed to the stretching vibration of sp-hybridized carbon [31]. The D band at around 1335 cm^{-1} comes from the defects and disorder structures of the carbonaceous solid, while the G band at around 1582 cm^{-1} corresponds to stretching of in-phase stretching vibration of sp^2 -hybridized carbon [32]. The intensity ratio of the D and G band ($I_{\text{D}}/I_{\text{G}}$) was 1.22 for N-doped γ -graphyne, which was higher than that of undoped γ -graphyne (0.66) [28], indicating more defects were



Scheme 1. Schematic illustration of (a) bias-free solar-driven electrocatalytic H_2O_2 generation, (b) electrocatalytic ORR, (c) traditional photocatalytic H_2O_2 generation.

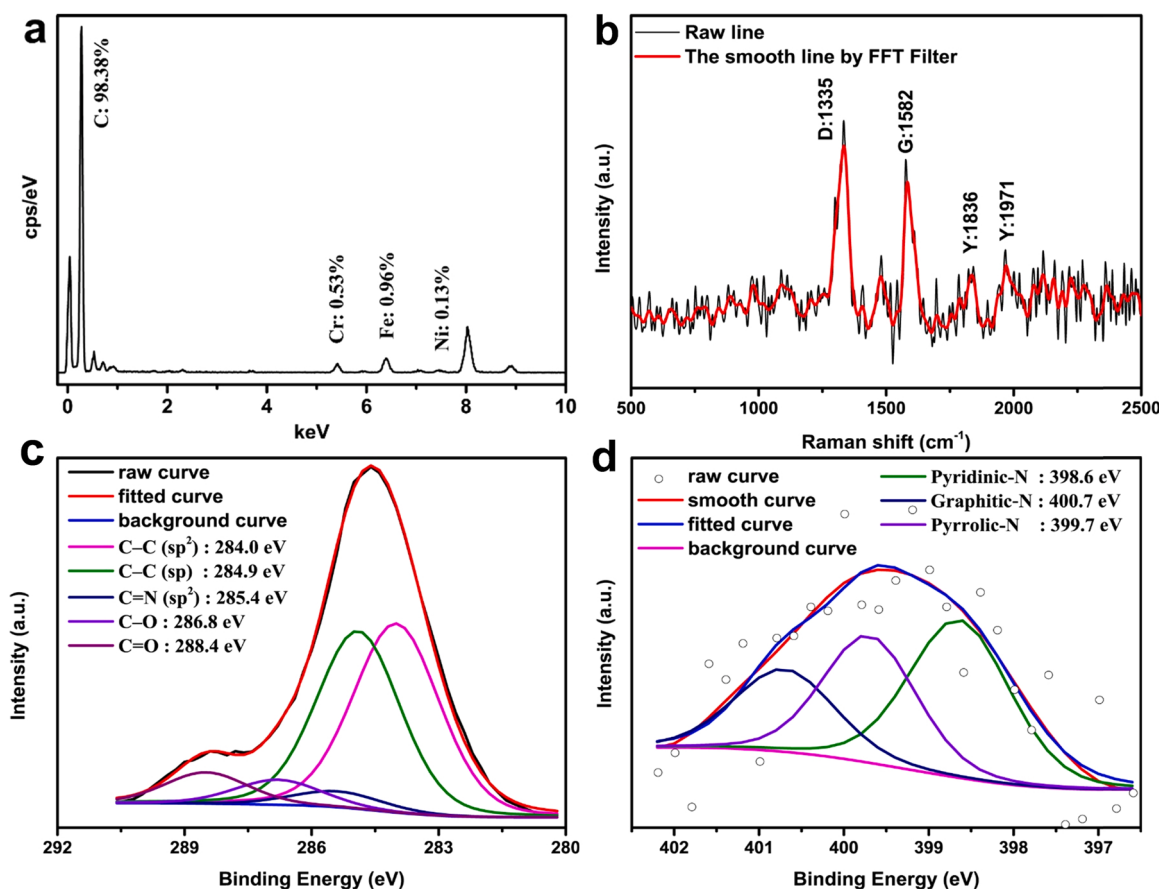


Fig. 1. Characterization of N-doped γ -graphyne. (a) EDX spectrum, (b) Raman spectrum, XPS (c) C1s and (d) N1s core-level spectra.

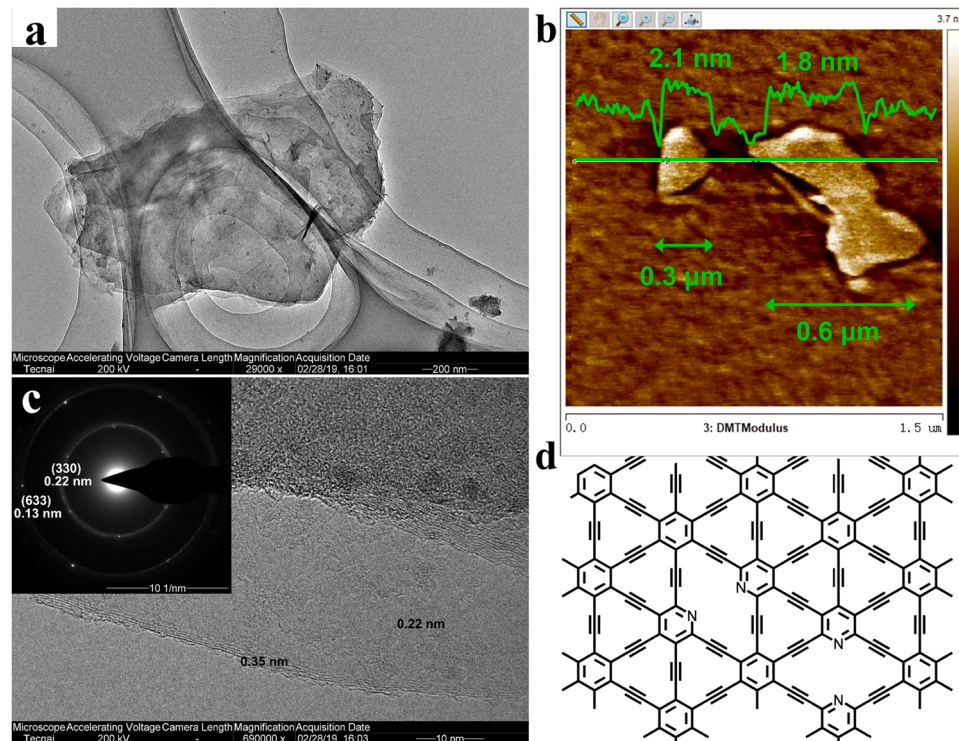


Fig. 2. Morphologies and microstructure of N-doped γ -graphyne. (a) TEM image, (b) AFM image, (c) HRTEM image (inset: SAED patterns), and (d) schematic illustration of the possible chemical structure.

introduced by N-doping. These results are accordant with the theoretical calculations [33] and experimental results from N-doped γ -graphdiyne [34–37].

The C1s core-level XPS spectrum of N-doped γ -graphyne was deconvoluted into five peaks at 284.0, 284.9, 285.4, 286.8, and 288.4 eV (Fig. 1c), indexing to the C 1s orbital of C=C(sp²), C≡C(sp), C=N(sp²), C–O(sp) and C=O(sp²), respectively [35–37]. The integral area ratio of sp-hybridized to sp²-hybridized carbon was around 1, which is consistent to the theoretical composition for γ -graphyne. The origin of oxygen should be associated with the surface-absorbed air [38], which has been reported in other graphyne materials [32–34]. The pyridinic-N (398.6 eV), pyrrolic-N (399.7 eV), and graphitic-N (400.7 eV) were assigned in the N1s core-level spectrum (Fig. 1d), revealing the presence of doped N [34,39]. The pyridinic-N originates from pyridine is widely considered as ORR active sites for carbon catalysts [40], while the graphitic-N and pyrrolic-N are usually reorganized during the annealing process due to their high thermal stability [41]. The molar content of pyridinic-N is 47.5%, which would be capable to greatly improve the ORR activities of the prepared N-doped γ -graphyne.

Fig. 2a shows a TEM image of the as-prepared N-doped γ -graphyne, in which a 2D overlapped nanosheets morphology with the size of 0.6–1 μ m can be observed. The size and thickness of nanosheets were further visualized by tapping-mode AFM imaging. The powders were dispersed in ethanol, diluted by a factor of 10¹⁰, and deposited onto the monocrystalline silicon pieces. As shown in Fig. 2b, the N-doped γ -graphyne exhibited a 2D structure with a size of around 0.3–0.6 μ m. A typical line profile was inserted to show the thickness of about 1.8–2.1 nm, corresponding to 5 or 6 layers of the N-doped γ -graphyne.

Theoretical calculations illustrated that γ -graphyne belongs to the hexagonal crystal system with hexagonal 2D crystal lattices of $a = b = 0.69$ nm [42,43]. SAED patterns were also measured for the as-prepared N-doped γ -graphyne, typical hexagonal diffraction spots coupled with diffraction rings were observed, indicating that the monocrystalline characteristic of γ -graphyne is destroyed to some degree with more defects after N doping. The diffraction spots/rings were indexed to (330) and (633) lattice planes. HRTEM image also reveals the (330) lattice plane according to the lattice fringes of 0.22 nm (Fig. 2c). An interlayer spacing of about 0.35 nm was observed at the edge of the N-doped γ -graphyne. Therefore, the as-prepared N-doped γ -graphyne consists of a 2D structure similar to γ -graphyne (Fig. 2d), and the N-doping sites are in-situ inherited from the pyridine precursors.

The band structure of the as-prepared N-doped γ -graphyne was determined by UV-vis DRS spectra and Mott-Schottky plots. The curve of transformed Kubelka-Munk function against photon energy was obtained from UV-vis DRS spectra illustrated the optical band gap of about

1.1 eV (Fig. S1a), which is consistent to the theoretical calculation that N-doped γ -graphyne was a semiconductor with an indirect band gap [44]. A negative slope was further observed in the Mott-Schottky plots (Fig. S1b), implying an n-type characteristic for the as-prepared sample. For an n-type semiconductor, the conduction band is usually close to the flat band potential. Thus, the conduction band of N-doped γ -graphyne was estimated to be around –1.04 V vs NHE. Fig. S2 drawn the energy band structure for the as-prepared N-doped γ -graphyne, the high level of the valence band might be in favor of restraining the oxidation of H₂O₂.

To explore the pristine ORR performance of N-doped γ -graphyne, N-doped γ -graphyne/GC electrode was employed as the working electrode in a three-electrode system. Fig. 3a shows the linear sweep voltammetry (LSV) curves in 0.1 M KOH electrolyte, at different rotation rates varying from 400 to 1600 rpm. The onset potential was 0.75 V vs RHE and one reduction peak could be observed at 0.43 V vs RHE, implying a 2e[–] reaction might happen if the applied potential is more positive than 0.43 V vs RHE. The electron transfer numbers (η) was calculated by Koutecky-Levich curves [45], as detailed in the Supporting Information. When the applied potential was more positive than 0.43 V vs RHE, the η was calculated to be approximately 2.5 at 0.43, 0.49, and 0.54 V vs RHE (Fig. 3b), which confirmed the 2e[–] transfer process. The relative error might be ascribed to the H-type electrolytic cell and turbulent flow. When the applied potential was more negative than 0.30 V vs RHE, the calculated η increased with the shift of applied potential from 0.30 to 0.10 V vs RHE (Fig. S3), illustrating the potential-dependent change of electron transfer process from 2e[–] to 4e[–]. The potential-dependent H₂O₂ selectivity was further confirmed by rotating ring-disk electrode (RRDE) [46] at 1600 rpm. As shown in Fig. S4, positive current could be observed on the Pt ring, illustrating the formation of H₂O₂. The corrected ring current (collection coefficient: 25%) approached to the disc current at the potential more positive than 0.7 V vs RHE, and did not increase with the increasing of disc current. Thus, N-doped γ -graphyne is expected to avoid the potential-dependent drop of H₂O₂ selectivity by working under a low overpotential.

3.2. H₂O₂ generation by bias-free solar-driven device

The ultimate objective for photosynthetic H₂O₂ generation is that H₂O₂ could be generated efficiently and cost-effectively without any sacrificial agents and bias. We employed TiO₂ electrodes as the photo-anode and wired the as-prepared N-doped γ -graphyne as the cathode to construct the bias-free solar-driven device (Fig. 4a) for H₂O₂ generation. TiO₂ is one of the most recognized photoanode materials with multiple advantages, including its low cost, earth abundance, and commercial availability. TiO₂ photoanode is an ideal choice for verifying the

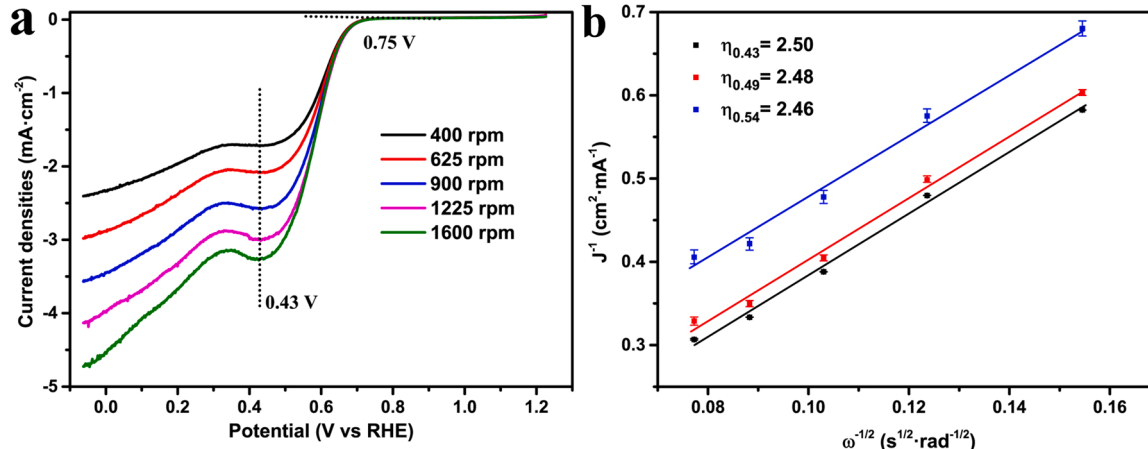


Fig. 3. (a) Rotating disk voltammograms of N-doped γ -graphyne in O₂-saturated 0.1 M KOH solution measured at various rotation rates. (b) corresponding Koutecky-Levich plots (J^{–1} versus $\omega^{-1/2}$) measured at 0.43, 0.49, and 0.54 V vs RHE; η denotes the electron transfer number.

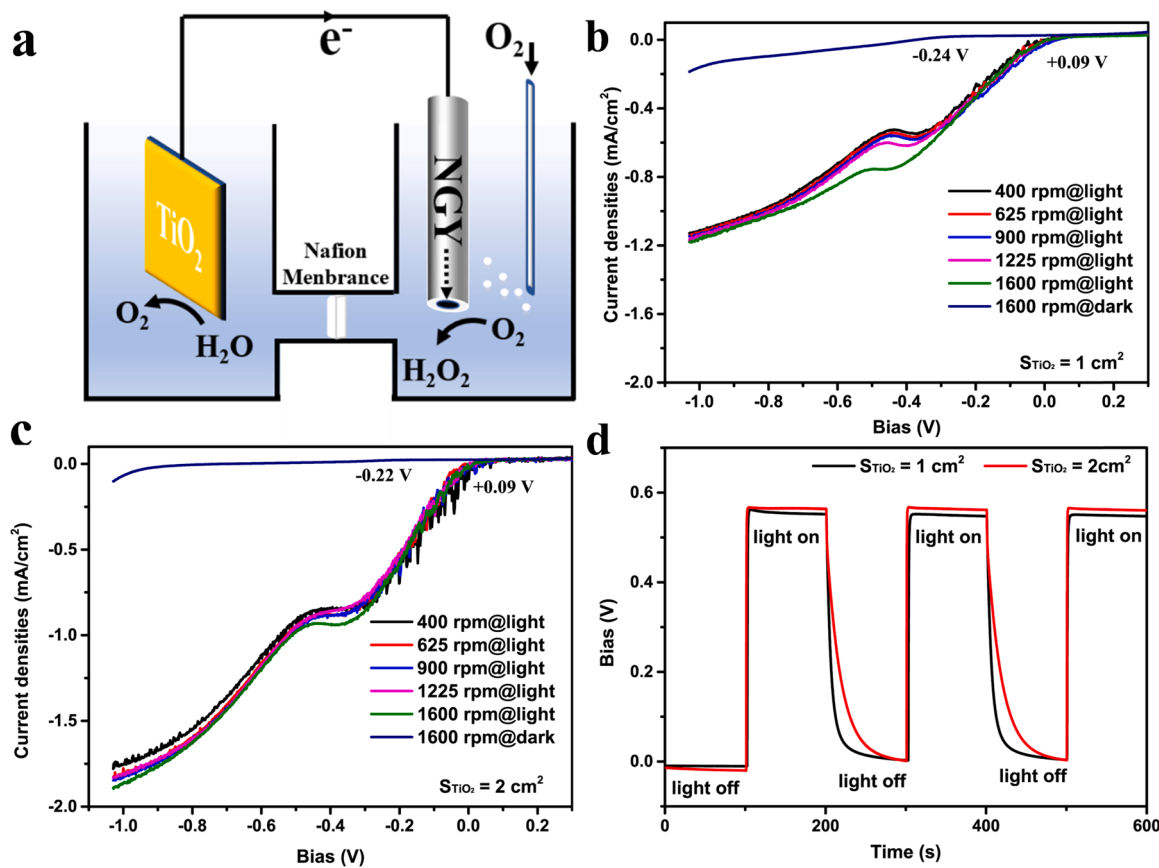


Fig. 4. (a) Illustration of the dual-electrode device with N-doped γ -graphyne as cathode and TiO_2 as photoanode in O_2 -saturated 0.1 M KOH solution. (b,c) Rotating disk voltammograms of the device under dark and irradiation with different areas of TiO_2 photoanode. (d) Open-circuit voltage of the device under intermittent illumination.

feasibility of the newly-developed PEC device. The synthesis and energy levels of the as-utilized TiO_2 are presented in Figs. S5 to S6.

Fig. 4b exhibits the LSV curves of the device under dark and irradiation. Under dark, ORR started at the bias of -0.24 V and the current density was very low. When the light was turned on, the bias for starting the ORR shifted towards $+0.09 \text{ V}$. Under the bias of 0 V , a negative current density was exhibited, indicating that ORR could happen with photo-induced electrons from the TiO_2 photoanode even with no bias. The appearance of reduction peaks illustrates that the ORR should be a $2e^-$ process with a bias lower than -0.3 V .

For this dual-electrode device, the current densities were no longer correlated with the rotating rate of RDE as the reaction was no longer a diffusion control. In order to study the rate-determining step, we increased the area of TiO_2 electrode from 1 to 2 cm^2 . The doubled photoanode area increased more photo-induced carriers under irradiation. As shown in Fig. 4c, the current densities under irradiation increased by 52%, indicating that the number of photo-induced carriers was the rate-determining step. Besides, the onset bias barely changed because the energy of the photo-induced electrons is constant for TiO_2 fabricated via the same method. The open-circuit voltage of the device under intermittent illumination also described the role of photo-induced electrons. As illustrated in Fig. 4d, the open-circuit voltage underwent a positive shift for ORR under irradiation, illustrating photo-induced electrons would lower the threshold of ORR. However, the open-circuit voltage did not shift according to the area of TiO_2 photoanode because increasing the area of photoanode would not contribute to the energy of photo-induced electrons, though the number of electrons increased.

In order to confirm the importance of the energy of photo-induced electrons, one Fe_2O_3 photoanode (1 cm^2) was used to take the place of

the TiO_2 photoanode for comparison. As shown in Figs. S7 to S9, the current densities were larger than those with the TiO_2 electrode (1 cm^2) as photoanode. This is reasonable because the bandgap of Fe_2O_3 is much narrower than that of TiO_2 , in which more photons could be absorbed and more photo-induced carriers would be generated. However, the onset bias was -0.10 V , indicating that the device could not produce H_2O_2 from ORR with 0 applied bias. This might be associated with the position of conduction band of Fe_2O_3 . The reduction ability of the photo-induced electrons produced by Fe_2O_3 photoanode is not as strong as those produced by TiO_2 photoanode because of its lower conduction level. Since the photo-induced carriers are the driving force of this device, the semiconductor photoanode materials (area and energy level) should be dominant factors in this unbiased device for photosynthetic H_2O_2 generation.

To demonstrate the bias-free H_2O_2 generation performance of the device, an H-type electrolytic cell with a Nafion membrane was employed (Fig. S10). The Nafion membrane isolated the TiO_2 photoanode and N-doped γ -graphyne cathode to prevent the generated H_2O_2 on cathode from being oxidized by anode during the reaction. The area of TiO_2 photoanode was further increased to 4 cm^2 according to the size of electrolytic cell in order to supply as many photo-induced electrons as possible. The influence of the light intensity was first studied. As shown in Fig. S11, stronger light irradiation induced larger current densities at the cathode electrode because the number of photons generated increased with increasing the light intensity ($83, 100, 130, 160, 186 \text{ mW}\cdot\text{cm}^{-2}$) under 0 bias. The onset bias also shifted towards more positive bias, illustrating stronger light irradiation would provide stronger driving force via more photo-induced carriers per unit area. Amperometric i-t curve of the device was then implemented with 0 V bias under irradiation ($\text{AM}1.5; 100 \text{ mW}\cdot\text{cm}^{-2}$) for 4 h (the upper limit of

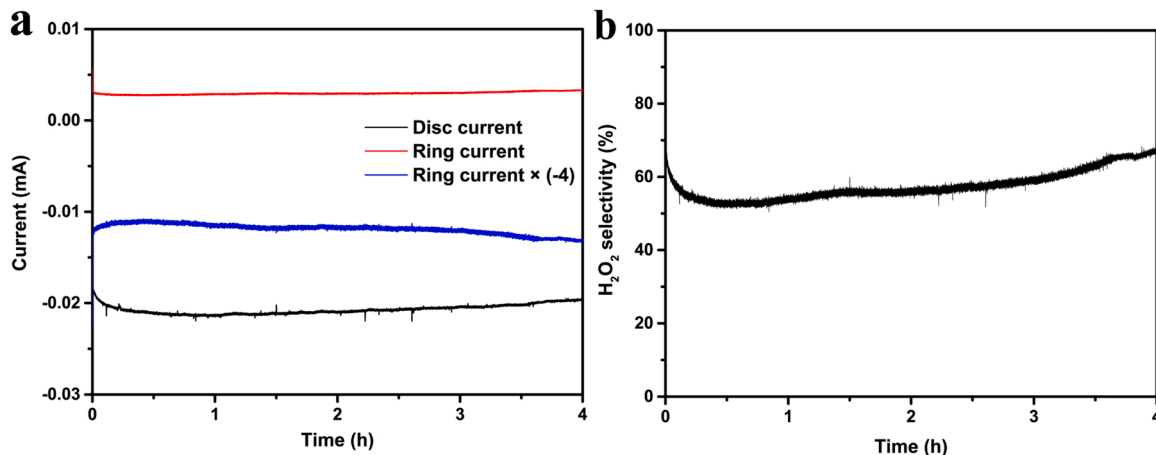


Fig. 5. (a) Amperometric i-t curve of the dual-electrode device implemented by rotating ring-disk electrode in O₂-saturated electrolytes under irradiation with 0 bias and (b) the H₂O₂ selectivity.

working time of our Xe lamp) in 0.1 mol·L⁻¹ KOH. The current density kept stable (Fig. 5a) and the H₂O₂ selectivity increased as the reaction progress (Fig. 5b).

3.3. The cyclic H₂O₂ generation activity

The device was operated for three circles to reveal the cyclic H₂O₂ generation activity. The charge-time curves (Fig. 6a) were relatively smooth during the whole reaction, despite the system disturbances of photocurrent. During cyclic reactions, the transfer of photo-induced electrons increased steadily. The H₂O₂ yield was measured by spectroscopic titration with H₂SO₄ solution (1 mol·L⁻¹) of KMnO₄ (10⁻⁴ mol·L⁻¹) according to the reaction: 2KMnO₄ + 5 H₂O₂ + 3 H₂SO₄ → K₂SO₄ + 2 MnSO₄ + 5 O₂ + 8 H₂O. Briefly, 2 mL KMnO₄ solution and 1 mL electrolyte were mixed and the absorbance at 526 nm and 545 nm was recorded by a UV-2300 UV-vis spectrophotometer. The yield of H₂O₂ was calculated by the calibration curve of KMnO₄ solution. The measured H₂O₂ yield efficiency reached as high as 7.47 mmol·h⁻¹ g⁻¹, outperformed previously-reported studies involving hole trapping agent (s) for the synthesis of H₂O₂ via traditional photocatalysis route (Table 1). Comparing to the ideal H₂O₂ yield calculated from the charge-time curve, H₂O₂ selectivity reached up to 74% (Fig. 6b), indicating an efficient 2e⁻ ORR for the N-doped γ -graphyne in this bias-free device.

The electrochemical active surface area (ECSA) of the N-doped γ -graphyne electrode before (Fig. 7a) and after (Fig. 7b) reaction were estimated to illustrate the stability and continuous improved H₂O₂

Table 1
Comparison of H₂O₂ generation with traditional photocatalysis route.

System	Light source	Time	Efficiency	References
N-doped γ -graphyne wired TiO ₂	Xe lamp	4 h	7.47 mmol·h ⁻¹ g ⁻¹	This work
Resorcinol-formaldehyde	Xe lamp	2 h	1.24 mmol·h ⁻¹ g ⁻¹	[47]
Au/TiO ₂	UV light	6 h	3.33 mmol·h ⁻¹ g ⁻¹	[48]
Pt/g-C ₃ N ₄	Xe lamp ($\lambda > 420$ nm)	1 h	0.17 mmol·h ⁻¹ g ⁻¹	[49]
Pt/g-C ₃ N ₄ + isopropanol	Xe lamp ($\lambda > 420$ nm)	1 h	1.24 mmol·h ⁻¹ g ⁻¹	[49]
Bi ₄ O ₅ Br ₂ /g-C ₃ N ₄	Xe lamp ($\lambda > 420$ nm)	1 h	2.48 mmol·h ⁻¹ g ⁻¹	[50]
g-C ₃ N ₄ -CoWO	Xe lamp ($\lambda > 420$ nm)	1 h	1.87 mmol·h ⁻¹ g ⁻¹	[51]
SN-GQD/TiO ₂ + 2-propanol	Xe lamp ($\lambda > 420$ nm)	1.5 h	3.31 mmol·h ⁻¹ g ⁻¹	[52]
holey defective g-C ₃ N ₄ + 2-propanol	Xe lamp ($\lambda > 420$ nm)	2.5 h	0.10 mmol·h ⁻¹ g ⁻¹	[53]
CdS-GO	Xe lamp ($\lambda > 420$ nm)	12 h	0.21 mmol·h ⁻¹ g ⁻¹	[54]
CoP/g-C ₃ N ₄ + ethanol	Xe lamp ($\lambda > 420$ nm)	2 h	1.40 mmol·h ⁻¹ g ⁻¹	[55]

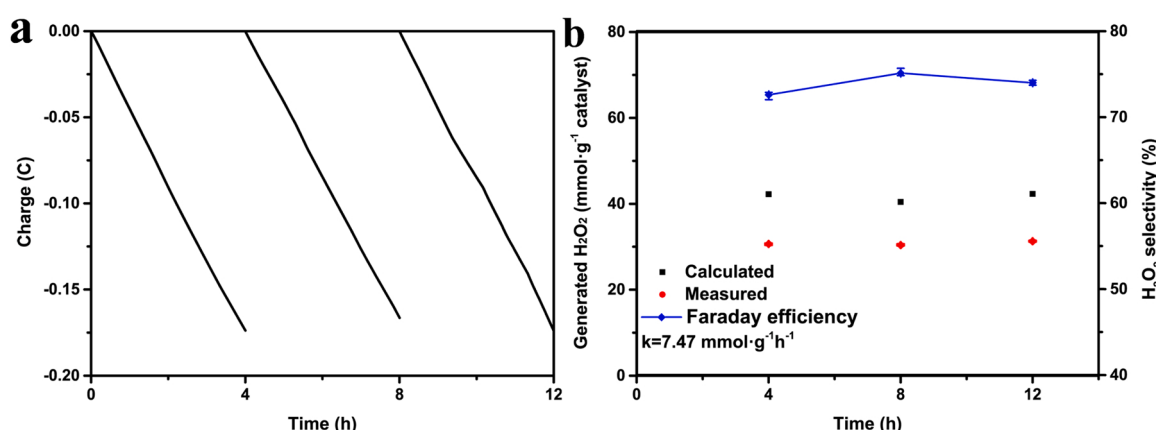


Fig. 6. (a) Charge-time curve of the dual-electrode device under 100 mW·cm⁻² irradiation at 0 bias during repeated operation cycles. (b) The measured H₂O₂ yield, the calculated H₂O₂ yield calculated from charge-time curve and H₂O₂ selectivity.

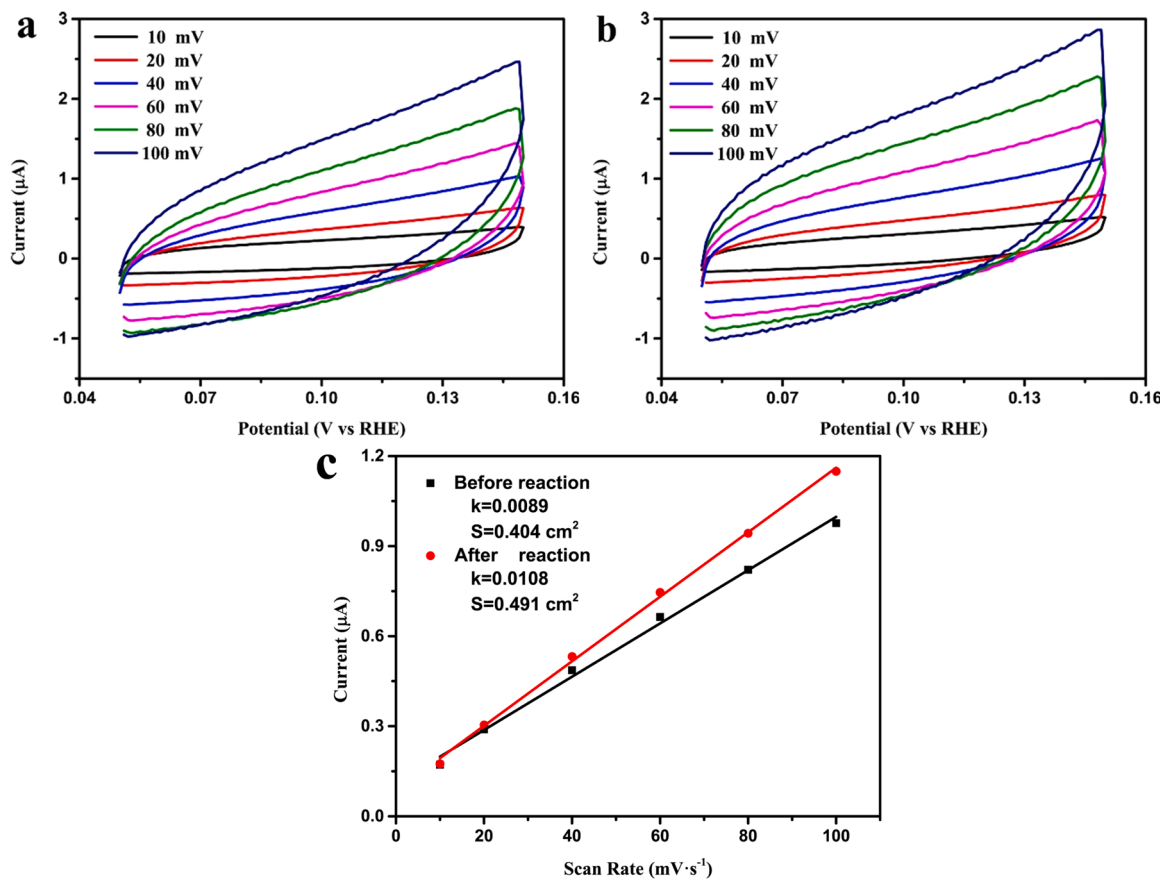


Fig. 7. Cyclic voltammograms of N-doped γ -graphyne@ glassy carbon electrode in $0.1 \text{ mol}\cdot\text{L}^{-1}$ KOH solution in a non-Faradaic region (a) before and (b) after cyclic ORR reaction. (c) The relationship between charging currents at 0.1 V vs SCE and scan rate.

selectivity. CV curves (three-electrode systems) were implemented under dark in $0.1 \text{ mol}\cdot\text{L}^{-1}$ KOH solution at different scan rates. A small potential window of $0.05\text{--}0.15 \text{ V}$ vs SCE was selected because N-doped γ -graphyne did not show any faradaic response within this window. The ECSA was calculated from the double-layer capacitance which was determined by the double-layer charging current (i_c) and scan rate (v): $\text{ECSA} = \frac{C_{DL}}{C_s} = \frac{i_c/v}{C_s}$, in which C_s was $22 \mu\text{F}\cdot\text{cm}^{-2}$ for carbon materials in alkaline solutions [56,57]. According to Fig. 7c, the ECSA increased 21.5% after cyclic reaction, illustrating the active sites of N-doped γ -graphyne were created (more exposed surface of N-doped γ -graphyne) during the cyclic H_2O_2 generation. A similar phenomenon has also been reported for γ -graphyne materials in our previous work [28]. The increasing ECSA may result from the continuous improvement of H_2O_2 generation on N-doped γ -graphyne with enhanced interfacial interactions between the electrode and electrolyte solution in this device since the lone pairs of electrons in N is beneficial to the absorbance of hydrogen ion.

3.4. Mechanisms

Density functional theory (DFT) calculations were carried out to understand the mechanism of the 2e^- ORR process on N-doped γ -graphyne. A molecular fragment of N-doped γ -graphyne (Fig. 8a) containing 116 carbon atoms and 2 nitrogen atoms was built as the model structure for the calculation. The accurate coordinates of these atoms after geometry optimization are presented in the Supporting Information. Then, the possible ORR pathways on N-doped γ -graphyne were proposed by assuming pyridinic-N, sp^2 -hybridized carbon, and sp^3 -hybridized carbon as active sites, respectively. Subsequently, the models of the possible reaction intermediates were built and their frequencies

were calculated with DMol3 module by the m-GGA M06-L functional. The detailed coordinates of the atoms in intermediates and the calculation results of total energy (Table S1) were supplied in the Supporting Information. Fig. 8b–d shows the relative energy of the possible reaction steps, in which the total energy of N-doped γ -graphyne at ground state was used as zero points. The energy change of the step of “NGY- OO^{2-} + $\text{H}_2\text{O} \rightleftharpoons \text{NGY}-\text{OOH}”$ is the highest, illustrating this step was the rate-determining reaction for 2e^- ORR. When pyridinic-N was introduced as the active sites (Fig. 8b), the energy change of this step was lowered greatly. The introduction of pyridinic-N would accelerate the slowest step of 2e^- ORR and improve the H_2O_2 generation efficiency for γ -graphyne. Furthermore, the total energy change of the proton abstraction would be smaller than the injection of the first electron when pyridinic-N played the role as active sites, which might be the reason for the high H_2O_2 selectivity.

The pH-dependence of N-doped γ -graphyne in this device was also unraveled. LSV curves and electrochemical impedance spectra of the device were investigated in O_2 -saturated electrolytes with different pH value. K_2SO_4 was employed as supporting electrolyte to guarantee the ionic strength constant at $0.1 \text{ mol}\cdot\text{L}^{-1}$. The current densities of the device showed a strong pH dependence (Fig. 9a). In acid electrolyte (H_2SO_4 solution) and neutral electrolyte (K_2SO_4 solution), the current densities increased gradually with the increase of pH values. In alkaline electrolyte (KOH solution), the onset bias underwent a positive shift while the current densities increased greatly with the increase of pH values. Thus, the device is expected to work in alkaline solution better and $0.1 \text{ mol}\cdot\text{L}^{-1}$ KOH is the most suitable electrolyte.

The Nyquist plots at 0 bias was implemented to analyze the charge transfer process at the interface. As displayed in Fig. 9c–d, one small semicircle at high frequencies and another large circular arc at low

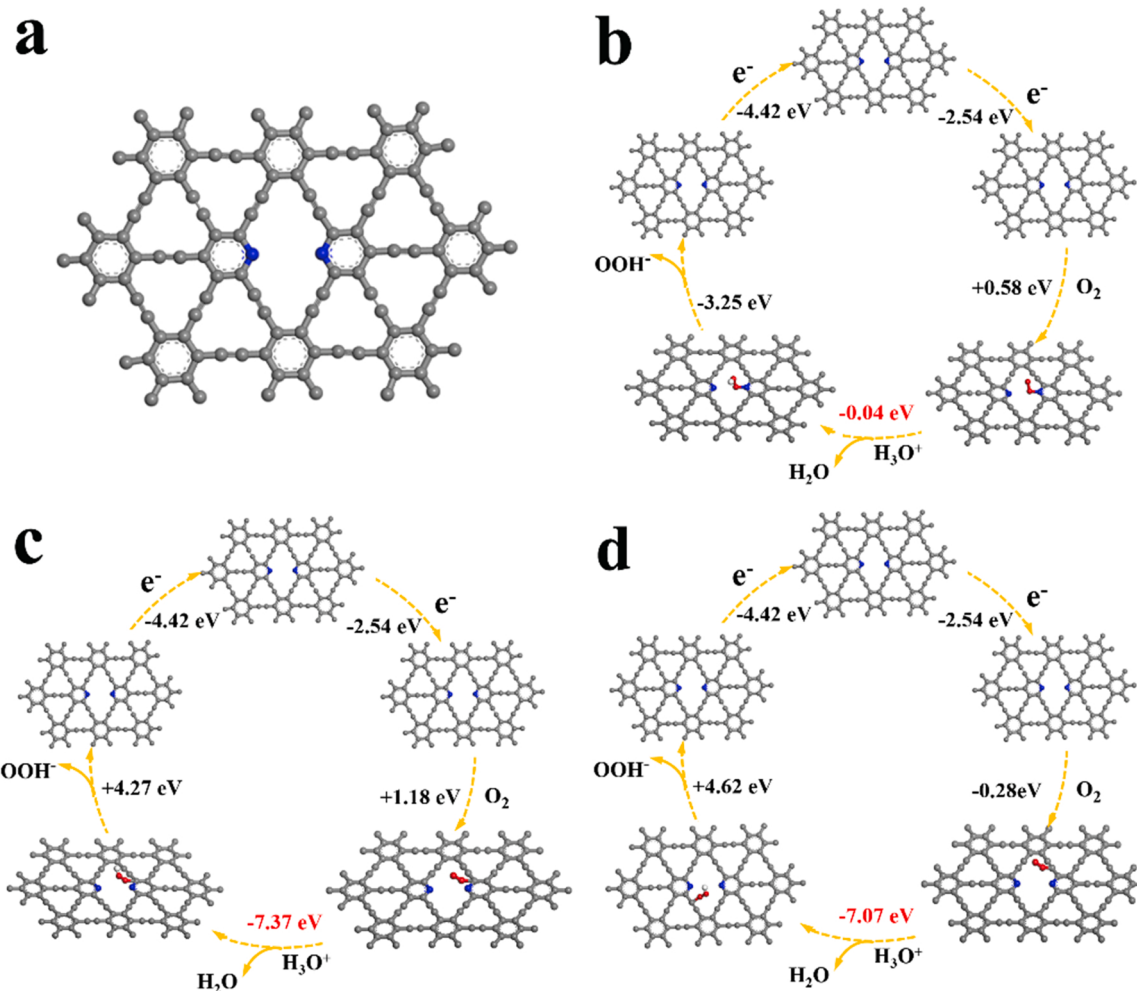


Fig. 8. (a) The model of N-doped γ -graphyne for calculation here and (b,c,d) the total energy profiles of key possible ORR pathways on N-doped γ -graphyne. The active site is (b) pyridinic-N, (c) sp^2 -hybridized carbon, and (d) sp -hybridized carbon, respectively.

frequencies were observed. The Nyquist plots were fitted according to the equivalent circuit model inserted in Fig. 9c and the fitting data were provided in Table S2. The R_i is the internal resistance; R_{ct1} and CPE1 is the resistance and constant phase element relevant to the smaller semicircle; R_{ct2} and CPE2 is the resistance and constant phase element related to the larger circular arc. The relationships between impedance and pH value were presented in Fig. 9b. The values of R_{ct2} were more than two orders of magnitudes larger than those of R_i and R_{ct1} , illustrating that R_{ct2} described the rate-determining step (the OER at photoanode, the ORR at cathode). R_{ct1} exhibited similar behavior in H₂SO₄ and KOH, which implied the corresponding processes were not sensitive to H⁺ or OH⁻ (the transport of photo-induced electrons). The values of R_{ct2} increased with the increase of pH values, which was consistent with the current densities in various electrolytes. The interfacial OER and ORR processes at electrodes were significantly influenced by electrolyte, contributing greatly to the pH-dependent performance of this solar-device.

The impact of the 1.62% stainless steel impurities was also considered. The impurities from the mechanical friction of ball-milling balls and pots are hard to completely avoid due to the characteristic of mechanochemistry. However, the mechano-synthesized sample has been etched by dilute nitric acid (0.1 mol·L⁻¹) several times under ultrasonic treatment during the days of etching process to remove stainless steel impurities on the surface. The residual impurities should be wrapped by the N-doped γ -graphyne because the stainless steel impurities that can interact with the acid etching solution must have been

removed. The undoped γ -graphyne synthesized by the same method also contained about 1% stainless steel impurities, but exhibited very poor ORR catalytic activity (Fig. S12), illustrating the contribution of stainless steel impurities, if any, could be neglected.

4. Conclusions

In summary, we have successfully synthesized in-situ N-doped γ -graphyne through a mechanochemical route and applied it for photosynthetic H₂O₂ generation. This newly-developed metal-free carbon material enabled the synthesis of H₂O₂ through 2e⁻ ORR in alkaline solution. The N-doped γ -graphyne electrode was wired with a TiO₂ photoanode and the onset bias of ORR was lowered up to 0.32 V. H₂O₂ was steadily produced under 0 bias with the irradiation of light. The H₂O₂ selectivity reached up to 74% and the H₂O₂ yield rate was as high as 7.47 mmol·h⁻¹g⁻¹ without any bias and sacrificial agent, outperformed previously reported syntheses of H₂O₂ via traditional photocatalytic routes with hole trapping agents. Theoretical calculations suggested that pyridinic-N in the N-doped γ -graphyne network is the active site, which lowered the rate-determining step of proton abstraction. In comparison with traditional photocatalytic H₂O₂ generation, the dual-working-electrode system developed in this study could promote the separation of photo-induced carriers and avoid the reversible reaction of H₂O₂ decomposition. The newly-developed methodology is rather general, which can be applied for photocatalytic reactions beyond the H₂O₂ generation.

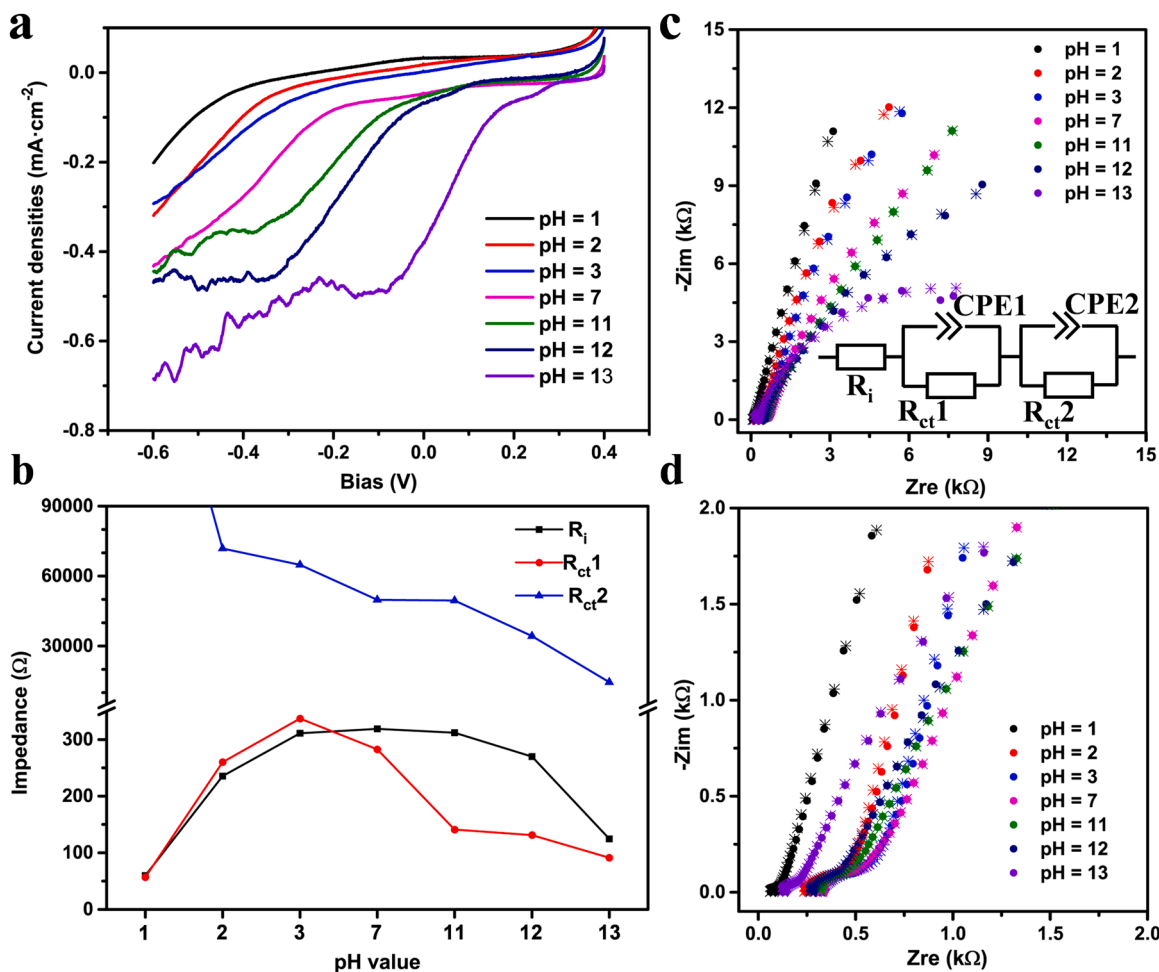


Fig. 9. (a) LSV curves, (b) the relationships between impedance and pH value, and the Nyquist plots (■ points) and fitting data (* points) of the dual-electrode device in O₂-saturated electrolytes with different pH values; (c) view of full frequencies, (d) enlarged view at high frequencies.

CRediT authorship contribution statement

Qiaodan Li: Methodology, Formal analysis, Investigation, Writing – original draft. **Yang Chen:** Validation, Resources, Writing – review & editing, Funding acquisition. **Feng Du:** Resources, Supervision. **Xiaoli Cui:** Conceptualization, Resources, Writing – review & editing, Project administration, Funding acquisition, Supervision. **Liming Dai:** Conceptualization, Resources, Project administration, Funding acquisition.

Declaration of Competing Interest

The authors declare that they have no known competing financial interests or personal relationships that could have appeared to influence the work reported in this paper.

Acknowledgements

This work was supported by the Natural Science Foundation of Shanghai (20ZR1403300), National Natural Science Foundation of China (52002076), China Scholarship Council, and Shaanxi Yanchang Petroleum (Group) Co., Ltd. LD is grateful for partial support from ARC (Australian Research Council, Australia) (DP 190103881, FL 190100126).

Appendix A. Supporting information

Supplementary data associated with this article can be found in the online version at doi:10.1016/j.apcatb.2021.120959.

References

- [1] G. Moon, W. Kim, A. Bokare, N. Sung, W. Choi, Solar production of H₂O₂ on reduced graphene oxide-TiO₂ hybrid photocatalysts consisting of earth-abundant elements only, Energy Environ. Sci. 7 (2014) 4023–4028, <https://doi.org/10.1039/C4EE02757D>.
- [2] T. Jeon, H. Kim, W. Choi, Highly durable photoelectrochemical H₂O₂ production via dual photoanode and cathode processes under solar simulating and external bias-free conditions, Energy Environ. Sci. 13 (2020) 1730–1742, <https://doi.org/10.1039/c9ee03154e>.
- [3] S. Fukuzumi, Y. Yamada, Hydrogen peroxide used as a solar fuel in one-compartment fuel cells, ChemElectroChem 3 (2016) 1978–1989, <https://doi.org/10.1002/celec.201600317>.
- [4] J. Ma, N.A. Choudhury, Y. Sahai, A comprehensive review of direct borohydride fuel cells, Renew. Sustain. Energy Rev. 14 (2010) 183–199, <https://doi.org/10.1016/j.rser.2009.08.002>.
- [5] K. Sato, M. Aoki, R. Noyori, A "Green" route to adipic acid: direct oxidation of cyclohexenes with 30 percent hydrogen peroxide, Science 281 (1998) 1646–1647, <https://doi.org/10.1126/science.281.5383.1646>.
- [6] S. Niwa, M. Eswaramoorthy, J. Nair, A. Raj, N. Itoh, H. Shoji, T. Namba, F. Mizukami, A one-step conversion of benzene to phenol with a palladium membrane, Science 295 (2002) 105–107, <https://doi.org/10.1126/science.1066527>.
- [7] Z. Teng, Q. Zhang, H. Yang, K. Kato, W. Yang, Y. Lu, S. Liu, C. Wang, A. Yamakata, C. Su, B. Liu, T. Ohno, Atomically dispersed antimony on carbon nitride for the artificial photosynthesis of hydrogen peroxide, Nat. Catal. 4 (2021) 374–384, <https://doi.org/10.1038/s41929-021-00605-1>.
- [8] M. Teranishi, S. Naya, H. Tada, In situ liquid phase synthesis of hydrogen peroxide from molecular oxygen using gold nanoparticle-loaded titanium (IV) dioxide

- photocatalyst, *J. Am. Chem. Soc.* 132 (2010) 7850–7851, <https://doi.org/10.1021/ja102651g>.
- [9] J. Campos-Martin, G. Blanco-Brieva, J. Fierro, Hydrogen peroxide synthesis: an outlook beyond the anthraquinone process, *Angew. Chem. Int. Ed.* 45 (2006) 6962–6984, <https://doi.org/10.1002/anie.200503779>.
- [10] J. Edwards, B. Solsona, E. Ntatinjua, A. Carley, A. Herzog, C. Kiely, G. Hutchings, Switching off hydrogen peroxide hydrogenation in the direct synthesis process, *Science* 323 (2009) 1037–1041, <https://doi.org/10.1126/science.1168980>.
- [11] D. Iglesias, A. Giuliani, M. Melchionna, S. Marchesan, A. Criado, L. Nasi, M. Bevilacqua, C. Tavagnacco, F. Vizza, M. Prato, P. Fornasiero, N-doped graphitized carbon nanohorns as a forefront electrocatalyst in highly selective O₂ reduction to H₂O₂, *Chem* 4 (2018) 106–123, <https://doi.org/10.1016/j.chempr.2017.10.013>.
- [12] L. Han, Y. Sun, S. Li, C. Cheng, C. Halbig, P. Feicht, J. Hübner, P. Strasser, S. Eigler, In-plane carbon lattice-defect regulating electrochemical oxygen reduction to hydrogen peroxide production over nitrogen-doped graphene, *ACS Catal.* 9 (2019) 1283–1288, <https://doi.org/10.1021/acscatal.8b03734>.
- [13] H. Kim, M. Ross, N. Kornienko, L. Zhang, J. Guo, P. Yang, B. McCloskey, Efficient hydrogen peroxide generation using reduced graphene oxide-based oxygen reduction electrocatalysts, *Nat. Catal.* (2018) 282–290, <https://doi.org/10.1038/s41929-018-0044-2>.
- [14] Y. Yi, L. Wang, G. Li, H. Guo, A review on research progress in the direct synthesis of hydrogen peroxide from hydrogen and oxygen: noble-metal catalytic method, fuel-cell method and plasma method, *Catal. Sci. Technol.* 6 (2016) 1593–1610, <https://doi.org/10.1039/C5CY01567G>.
- [15] Y. Qiu, W. Liu, W. Chen, W. Chen, G. Zhou, P. Hsu, R. Zhang, Z. Liang, S. Fan, Y. Zhang, Y. Cui, Efficient solar-driven water splitting by nanocone BiVO₄-perovskite tandem cells, *Sci. Adv.* 2 (6) (2016) 1501764, <https://doi.org/10.1126/sciadv.1501764>.
- [16] M. Jakešová, D. Apaydin, M. Sytnyk, K. Oppelt, W. Heiss, N. Sariciftci, E. Glowacki, Hydrogen-bonded organic semiconductors as stable photoelectrocatalysts for efficient hydrogen peroxide photosynthesis, *Adv. Funct. Mater.* 26 (2016) 5248–5254, <https://doi.org/10.1002/adfm.201601946>.
- [17] D. Du, S. Zhao, Z. Zhu, F. Li, J. Chen, Photo-excited oxygen reduction and oxygen evolution reactions enable a high-performance Zn-Air battery, *Angew. Chem. Int. Ed.* 132 (41) (2020) 18297–18301, <https://doi.org/10.1002/ange.202005929>.
- [18] K. Sokol, W. Robinson, J. Warnan, N. Kornienko, M. Nowaczyk, A. Ruff, J. Zhang, E. Reisner, Bias-free photoelectrochemical water splitting with photosystem II on a dye-sensitized photoanode wired to hydrogenase, *Nat. Energy* 3 (2018) 944–951, <https://doi.org/10.1038/s41560-018-0232-y>.
- [19] H. Zhang, H. Wang, J. Xuan, Rational design of photoelectrochemical cells towards bias-free water splitting: Thermodynamic and kinetic insights, *J. Power Sources* 462 (2020), 228113, <https://doi.org/10.1016/j.jpowsour.2020.228113>.
- [20] H. Kim, S. Bae, D. Jeon, J. Ryu, Fully solution-processable Cu₂O-BiVO₄ photoelectrochemical cells for bias-free solar water splitting, *Green Chem.* 20 (2018) 3732–3742, <https://doi.org/10.1039/c8gc00681d>.
- [21] B. Zhang, S. Wang, W. Fan, W. Ma, Z. Liang, J. Shi, S. Liao, C. Li, Photoassisted oxygen reduction reaction in H₂-O₂ fuel cells, *Angew. Chem. Int. Ed.* 128 (47) (2016) 14968–14971, <https://doi.org/10.1002/ange.201607118>.
- [22] W. Fan, B. Zhang, X. Wang, W. Ma, D. Li, Z. Wang, M. Dupuis, J. G. Shi, S. Liao, C. Li, Efficient hydrogen peroxide synthesis by metal-free polyterthiophene via photoelectrocatalytic dioxygen reduction, *Energy Environ. Sci.* 13 (2020) 238–245, <https://doi.org/10.1039/C9EE02247C>.
- [23] R. Baughman, H. Eckhardt, M. Kertesz, Structure-property predictions for new planar forms of carbon: layered phases containing sp² and sp atoms, *J. Chem. Phys.* 87 (1987) 6687–6699, <https://doi.org/10.1063/1.453405>.
- [24] A. Hirsch, The era of carbon allotropes, *Nat. Mater.* 9 (2010) 868–871, <https://doi.org/10.1038/nmat2885>.
- [25] Q. Li, Y. Li, Y. Chen, L. Wu, C. Yang, X. Cui, Synthesis of γ-graphyne by mechanochemistry and its electronic structure, *Carbon* 136 (2018) 248–254, <https://doi.org/10.1016/j.carbon.2018.04.081>.
- [26] L. Wu, Q. Li, C. Yang, X. Ma, Z. Zhang, X. Cui, Constructing a novel TiO₂/γ-graphyne heterojunction for enhanced photocatalytic hydrogen evolution, *J. Mater. Chem. A* 6 (2018) 20947–20955, <https://doi.org/10.1039/C8TA07307D>.
- [27] B. Gao, M. Sun, W. Ding, Z. Ding, W. Liu, Decoration of γ-graphyne on TiO₂ nanotube arrays: improved photoelectrochemical and photoelectrocatalytic properties, *Appl. Catal. B Environ.* 281 (2021), 119492, <https://doi.org/10.1016/j.apcatb.2020.119492>.
- [28] Q. Li, C. Yang, L. Wu, H. Wang, X. Cui, Converting benzene into γ-graphyne and its enhanced electrochemical oxygen evolution performance, *J. Mater. Chem. A* 7 (2019) 5981–5990, <https://doi.org/10.1039/C8TA10317H>.
- [29] C. Yang, Y. Li, Y. Chen, Q. Li, L. Wu, X. Cui, Mechanochemical synthesis of γ-graphyne with enhanced lithium storage performance, *Small* 15 (8) (2019) 1804710, <https://doi.org/10.1002/smll.201804710>.
- [30] Y. Chen, Q. Li, W. Wang, Y. Lu, C. He, D. Qiu, X. Cui, Constructing ordered rhombic channels in graphyne analogues for potassium-ion storage, *2D Mater.* 8 (4) (2021), 044012, <https://doi.org/10.1088/2053-1583/ac26dc>.
- [31] J. Li, Z. Xie, Y. Xiong, Z. Li, Q. Huang, S. Zhang, Architecture of β-graphdiyne-containing thin film using modified Glaser-Hay coupling reaction for enhanced photocatalytic property of TiO₂, *Adv. Mater.* 29 (2017) 1700421, <https://doi.org/10.1002/adma.201700421>.
- [32] Y. Li, Q. Liu, W. Li, Y. Lu, H. Meng, C. Li, Efficient destruction of hexachlorobenzene by calcium carbide through mechanochemical reaction in a planetary ball mill, *Chemosphere* 166 (2017) 275–280, <https://doi.org/10.1016/j.chemosphere.2016.09.135>.
- [33] S. Zhang, J. Wang, Z. Li, R. Zhao, L. Tong, Z. Liu, J. Zhang, Z. Liu, Raman spectra and corresponding strain effects in graphyne and graphdiyne, *J. Phys. Chem. C* 120 (2016) 10605–10613, <https://doi.org/10.1021/acs.jpcc.5b12388>.
- [34] Z. Yang, X. Shen, N. Wang, J. He, X. Li, X. Wang, Z. Hou, K. Wang, J. Gao, T. Jiu, C. Huang, Graphdiyne containing atomically precise N atoms for efficient anchoring of lithium ion, *ACS Appl. Mater. Interfaces* 11 (2019) 2608–2617, <https://doi.org/10.1021/acsami.8b01823>.
- [35] S. Zhang, H. Du, J. He, C. Huang, H. Liu, G. Cui, Y. Li, Nitrogen-doped graphdiyne applied for lithium-ion storage, *ACS Appl. Mater. Interfaces* 8 (2016) 8467–8473, <https://doi.org/10.1021/acsami.6b00255>.
- [36] H. Shang, Z. Zuo, H. Zheng, K. Li, Z. Tu, Y. Yi, H. Li, Y. Li, Y. Li, N-doped graphdiyne for high-performance electrochemical electrodes, *Nano Energy* 44 (2018) 144–154, <https://doi.org/10.1016/j.nanoen.2017.11.072>.
- [37] X. Kan, Y. Ban, C. Wu, Q. Pan, H. Liu, J. Song, Z. Zuo, Z. Li, Y. Zhao, Interfacial synthesis of conjugated two-dimensional N-graphdiyne, *ACS Appl. Mater. Interfaces* 10 (2018) 53–58, <https://doi.org/10.1021/acsami.7b17326>.
- [38] S. Geng, S. Zhang, H. Onishi, XPS applications in thin films research, *Mater. Technol.* 17 (2002) 234–240, <https://doi.org/10.1080/10667857.2002.11752992>.
- [39] Y. Zhao, J. Wan, H. Yao, L. Zhang, K. Lin, L. Wang, N. Yang, D. Liu, L. Song, J. Zhu, L. Gu, L. Liu, H. Zhao, Y. Li, D. Wang, Few-layer graphdiyne doped with sp-hybridized nitrogen atoms at acetylénic sites for oxygen reduction electrocatalysis, *Nat. Chem.* 10 (2018) 924–931, <https://doi.org/10.1038/s41557-018-0100-1>.
- [40] Y. Jia, L. Zhang, L. Zhuang, H. Liu, X. Yan, X. Wang, J. Liu, J. Wang, Y. Zheng, Z. Xiao, E. Tarhan, J. Chen, D. Yang, Z. Zhu, S. Wang, L. Dai, X. Yao, Identification of active sites for acidic oxygen reduction on carbon catalysts with and without nitrogen doping, *Nat. Catal.* 2 (2019) 688–695, <https://doi.org/10.1038/s41929-019-0297-4>.
- [41] Y. Yue, Y. Xu, F. Kong, Q. Li, S. Ren, Bulk-synthesis and supercapacitive energy storage applications of nanoporous triazine-based graphdiyne, *Carbon* 167 (15) (2020) 202–208, doi: j.carbon.2020.06.001.
- [42] A. Puigdollers, G. Alonso, P. Gamallo, First-principles study of structural, elastic and electronic properties of α-, β- and γ-graphyne, *Carbon* 96 (2016) 879–887, <https://doi.org/10.1016/j.carbon.2015.10.043>.
- [43] P. Jiang, H. Liu, L. Cheng, D. Fan, J. Zhang, J. Wei, Thermoelectric properties of graphyne from first-principles calculations, *Carbon* 113 (2016) 108–113, <https://doi.org/10.1016/j.carbon.2016.11.038>.
- [44] A. Ruiz-Puigdollers, P. Gamallo, DFT study of the role of N- and B-doping on structural, elastic and electronic properties of α-, β- and γ-graphyne, *Carbon* 114 (2017) 301–310, <https://doi.org/10.1016/j.carbon.2016.12.026>.
- [45] Y. Zhang, T. Han, J. Fang, P. Xu, X. Li, J. Xu, C. Liu, Integrated Pt₂Ni alloy@Pt core-shell nanoarchitectures with high electrocatalytic activity for oxygen reduction reaction, *J. Mater. Chem. A* 2 (2014) 11400–11407, <https://doi.org/10.1039/C4TA00731J>.
- [46] R. Zhou, Y. Zheng, M. Jaroniec, S. Qiao, Determination of the electron transfer number for the oxygen reduction reaction: from theory to experiment, *ACS Catal.* 6 (2016) 4720–4728, <https://doi.org/10.1021/acscatal.6b01581>.
- [47] Y. Shiraishi, T. Takii, T. Hagi, S. Mori, Y. Kofuji, Y. Kitagawa, S. Tanaka, S. Ichikawa, T. Hirai, Resorcinol-formaldehyde resins as metal-free semiconductor photocatalysts for solar-to-hydrogen peroxide energy conversion, *Nat. Mater.* 18 (2019) 985–993, <https://doi.org/10.1038/s41563-019-0398-0>.
- [48] M. Teranishi, S. Naya, H. Tada, In situ liquid phase synthesis of hydrogen peroxide from molecular oxygen using gold nanoparticle-loaded titanium(iv) dioxide photocatalyst, *J. Am. Chem. Soc.* 132 (2010) 7850–7851, <https://doi.org/10.1021/ja102651g>.
- [49] X. Dang, R. Yang, Z. Wang, S. Wu, H. Zhao, Efficient visible-light activation of molecular oxygen to produce hydrogen peroxide using P doped g-C₃N₄ hollow spheres, *J. Mater. Chem. A* 8 (2020) 22720–22727, <https://doi.org/10.1039/DOTA07794A>.
- [50] X. Zhao, Y. You, S. Huang, Y. Wu, Y. Ma, G. Zhang, Z. Zhang, Z-scheme photocatalytic production of hydrogen peroxide over Bi₄O₅Br₂/g-C₃N₄ heterostructure under visible light, *Appl. Catal. B Environ.* 278 (2020), 119251, <https://doi.org/10.1016/j.apcatb.2020.119251>.
- [51] S. Zhao, X. Zhao, Insights into the role of singlet oxygen in the photocatalytic hydrogen peroxide production over polyoxometalates-derived metal oxides incorporated into graphitic carbon nitride framework, *Appl. Catal. B Environ.* 250 (2019) 408–418, <https://doi.org/10.1016/j.apcatb.2019.02.031>.
- [52] L. Zheng, H. Su, J. Zhang, L.S. Walekar, H.V. Molamahood, B. Zhou, M. Long, Y. H. Hu, Highly selective photocatalytic production of H₂O₂ on sulfur and nitrogen co-doped graphene quantum dots tuned TiO₂, *Appl. Catal. B Environ.* 239 (2018) 475–484, <https://doi.org/10.1016/j.apcatb.2018.08.031>.
- [53] L. Shi, L. Yang, W. Zhou, Y. Liu, L. Yin, X. Hai, H. Song, J. Ye, Photoassisted construction of holey defective g-C₃N₄ photocatalysts for efficient visible-light-driven H₂O₂ production, *Small* 14 (2018) 1703142, <https://doi.org/10.1002/smll.201703142>.
- [54] S. Thakur, T. Kshetri, N.H. Kim, J.H. Lee, Sunlight-driven sustainable production of hydrogen peroxide using a CdS-graphene hybrid photocatalyst, *J. Catal.* 345 (2017) 78–86, <https://doi.org/10.1016/j.jcat.2016.10.028>.
- [55] Y. Peng, L. Wang, Y. Liu, H. Chen, J. Lei, J. Zhang, Visible-light-driven photocatalytic H₂O₂ production on g-C₃N₄ loaded with CoP as a noble metal free

- cocatalyst, *Eur. J. Inorg. Chem.* (2017) 4797–4802, <https://doi.org/10.1002/ejic.201700930>.
- [56] C. McCrory, S. Jung, J. Peters, T. Jaramillo, Benchmarking heterogeneous electrocatalysts for the oxygen evolution reaction, *J. Am. Chem. Soc.* 135 (2013) 16977–16987, <https://doi.org/10.1021/ja407115p>.
- [57] T. Centeno, F. Stoeckli, On the specific double-layer capacitance of activated carbons, in relation to their structural and chemical properties, *J. Power Sources* 154 (2006) 314–320, <https://doi.org/10.1016/j.jpowsour.2005.04.007>.